Study of radiative shocks using 2D interferometry and XUV spectroscopy

R L Singh, C. Stehlé, M. Kozlova, M. Cotelo, J. Dostal, R. Dudzák, R. Rodriguez, P. Velarde, P. Barroso, F. Suzuki-Vidal, et al.

Study of Radiative shocks using 2D interferometry and XUV spectroscopy

R. L. Singh,[1] C. Stehlé,[2] M. Kozlova,[1,3] M. Cotelo,[4] J. Dostal,[5,3] R. Dudzák,[5,3] R. Rodriguez,[6] P. Velarde,[4] P. Barroso,[7] F. Suzuki-Vidal,[8] and T. Pisarczyk[9]

[1)] *Extreme Light Infrastructure ERIC, ELI-Beamlines Facility,25241 Dolní Břežany, Czech Republic*

[2)] *LERMA, Sorbonne-Université, Observatoire de Paris, CNRS, France*

[3)] *Institute of Plasma Physics, Czech Academy of Science, Prague, Czech Republic*

[4)] *Instituto de Fusion Nuclear Guillermo Velarde, Universidad Pôlitécnica de Madrid, Madrid, Spain*

[5)] *Institute of Physics of the Czech Academy of Sciences, Na Slovance 1999/2, 182 21 Prague, Czech Republic*

[6)] *Universidad de Las Palmas de Gran Canaria, Las Palmas de Gran Canaria, Spain*

[7)] *GEPI, Observatoire de Paris, Université PSL, CNRS, Place Jules Janssen F-92195, Meudon, France*

[8)] *First Light Fusion Ltd., Oxford, UK*

[9)] *The Institute of Plasma Physics and Laser Microfusion, Warsaw, Poland*

(*Electronic mail: raj.laxmisingh@eli-beams.eu; raaj.phys@gmail.com)

(Dated: 23 November 2023)

We report new experimental results on radiative shocks obtained in Xenon and Argon in gas cells at two different pressures below 1 bar. These shock waves are generated by the interaction of the PALS iodine laser on a CH-Au foil with a typical velocity in the range of 50 – 100 km/s depending on the variable laser intensity, pressure and gas. Attention is paid to the morphology and the dynamics of the radiative precursor over large time scales up to 30 ns, using 2D sub-picosecond visible interferometry, illustrating the complex interplay of hydrodynamic and radiation absorption for different initial conditions. The comparison between 1D and 2D simulations confirms the role played by lateral radiative losses in the ionization wave and the necessity of state-of-the-art integrated opacities. This study is complemented by the first XUV analysis of the shock emission between 5 and 20 nm obtained with a grating spectrometer, with line identification, which are compatible with the ionization stages deduced from interferometry and simulations.

I. INTRODUCTION

Radiative shocks occur at large velocities (compared to the sound velocity) such that high temperatures are obtained in the compressed matter[1]. They are characterized by a strong coupling between hydrodynamics and radiation[2]. At low densities, the radiation, which escapes from the structure, acts as a cooling mechanism. At higher densities, this radiation emitted by the hot post-shock may be partly absorbed, particularly by the colder gas in which the shock propagates. This leads to the development of a radiative precursor preceding the density discontinuity. Such precursors are visible in various circumstances, for instance, the top of high velocity (several 100 km/s) stellar jets propagating in the interstellar medium[3], in the case of accretion shocks[4,5], or when the shocks emerge from the atmosphere of exploding supernovae[6,7].

Radiative shocks have been the objects of many theoretical works[2,8–11]. They are considered as a test case of coupling between radiation and hydrodynamic[12–15], which in turn need to be tested against dedicated experiments. Besides few experiments performed on electric pulsed power installations[16–18], the majority of the experiments have been performed on high energy nanosecond laser installations[19–27], with laser intensity on the target of about 10^{14} W/cm^2. As radiative effects increase with the Mach Number, most experiments have been performed in heavy gases like Xenon, at various initial pressures, where typical shock velocities are in the range of 50 km/s and are analysed over a few nanoseconds.

As a consequence of a large number of ionisation stages and excitation levels, the strong shocks in heavy gases are characterized by a high post-shock compression, which may exceed 10^1 compared to the adiabatic gas compression of 4. Thus the shock velocity remains closer to the piston velocity. This effect is reinforced by radiation cooling[21]. Besides this, the most important signature of these shocks is the development of a radiative precursor ahead of the shock front which is the consequence of the radiation absorption during its transfer in the unshocked gas.

Numerical simulations of these phenomena have been often performed using 1D radiative hydrodynamical simulations[20,28]. If such simulations present the interest to provide useful indications about the plasma conditions, however, as shown earlier, to compare more precisely with the experiments, 2D simulations are necessary, even if the plasma is confined within the target boundaries[14,15,22,24]. All these simulations are strongly dependent on the quality of the Planck and Rosseland averaged opacities[29].

A complete view of these shocks would require an image of both the thin postshock layer and the more extended radiative precursor. The best candidate for this is the combination of XUV imaging, which allowed us to visualize both the post-shock and the high-density region of the precursor[24]. If few experiments were able to show the development of instabilities in the post-shock region through high-resolution X-ray imaging[25], most experiments concentrated on the radiative precursor[22,30] using visible techniques. However, there is a lack of systematic study of the effect of the initial pressure, gas nature and laser intensity on the target, which is one of the objectives of the present study, using time-resolved visible interferometry. This diagnostic enables us to visualise for

the various conditions (nature of the gas, pressure, focal spot and laser energy) the space and time evolution of the radiative precursor, through the measurement of its electron density.

Interestingly, although shock spectroscopic signatures are widely used in astrophysics, their study remains experimentally poor for shocks generated by lasers[22,26]. However, as in astrophysics, they could be indicators of the shock velocity by the Doppler effect, of the plasma temperature. In some cases of temperatures exceeding the millions of degrees, NLTE effects should also be considered. Whereas radiative transfer in the lines has often been taken into account for interpreting many astronomical observations, this last aspect is today not taken into account experimentally, due to the challenge in spectroscopic detection. To increase the bridge with astrophysical shocks, it is now necessary to complete these experimental works with the analysis of their spectroscopic signatures. This aspect remains today challenging and has never been touched on in detail. A first step in this direction will be proposed in the present work.

In this context, our work concerns a comparative study of laser-generated shock waves obtained at the PALS laser facility, with a focus on the radiation effects on the shock topology, dynamics and their signatures for two different noble gases (Argon and Xenon) at two different pressures and for different laser conditions. Several questions motivate this study: is the precursor development faster for the lighter gas? For a lower pressure? Is the ionisation wave monotonically decreasing with time? What is the influence of the diameter of the laser focal spot? What is the effect of the walls? What are the influences of opacity on the dynamics and topology and dynamics of the precursor for the same initial laser conditions? What are the expected spectral signatures of the shock? Is it possible to obtain detailed spectroscopic data?

II. EXPERIMENTAL SETUP

The experiment was performed at the kJ PALS iodine laser facility[31]. An overall layout of the experiment is presented in figure 1. The 4 mm long parallelepipedic gas cell target is closed by a coated CH foil at one end and by a brass disk on the opposite side. The Au-CH foil acts as a piston to launch the shock. The target cells were filled with noble gases (Xe, Xe+He (90 -10 % mixture) or Ar) at a pressure between 0.2 and 0.6 bar.

The laser (438 nm, 0.35 ns) with energy 100-180 J at 3ω was focused on the Au-CH foil of the target with a focus size of about 250-350 μm. Typical laser peak intensity is $\sim 4\times10^{14}$ W/cm^2 for 350 μm focal spot and energy 145 J.

Due to the incidence of the laser on the Au-CH foil, the shock was launched and propagated in the gas cell toward the closing disk. This shock propagation was recorded using visible interferometry and XUV spectroscopy. The CH (Parylene-N; 10 μm) foil was used as an ablator during the laser-matter interaction and the thin layer of Au (580 nm) was placed on the side of the interior of the tube, aiming at preventing X-ray radiation. The top window of the target was made of a 100 nm thick Si_3N_4 window supported by a 0.2 mm thick Si frame to

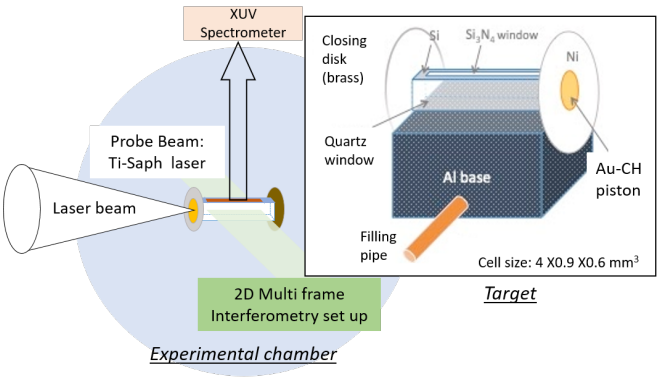

FIG. 1. Layout of the experimental setup and target (in the inset). The laser beam (0.3 ns, 100-180 J, 430 nm) focuses on the CH layer of the Au-CH piston of the target. An XUV spectrometer looks from the top through the SiN window of the target. The direction of the Ti-Saph probe beam for the 2D interferometry is presented in the schematic in green colour. It propagates through the two lateral quartz windows.

pass the shock XUV radiation toward the XUV spectrometer. The two lateral windows, separated by a distance of 0.6 mm, were made of 0.5 mm thick quartz with anti-reflective visible coating and were thus adapted to the visible interferometric diagnostic (see figure 1). The details of these diagnostics setups are presented in the following subsections.

As indicated previously, two different noble gases (Xe and Ar) were studied to inspect the variation of the radiative shock (speed and structure) versus the atomic number: pure Xenon, a mixture of XeHe (90/10% in the number of atoms) and Argon. The inclusion of a small proportion of Helium was chosen for comparison with an earlier study[26] showing that the presence of the lines of He^+ is a complementary indicator of the plasma temperature. This small quantity of Helium affects marginally the shock dynamics compared to the case for pure Xenon. The gas pressure varied between 0.2 and 0.6 bar.

A. Visible Interferometry

A Ti: Saph laser (wavelength: 811 nm, diameter: 30 mm, energy < 1 mJ and pulse duration > 40 fs) was used in the visible interferometry imaging setup. This laser was synchronized with the PALS beam.[32].

The probing laser was separated into three independent beams, with different angles between them, spaced by 3°. With this setup, we could record the images between 3 ns to 30 ns with its initial time t_0 (launch of the shock). An optical delay is implemented between these three interferometric arms to provide images of the moving shock at three times separated by 12 ns. Each interferometer is based on the half Fresnel bi-prism (a layout of this setup is presented in figure 2 of Kasperczuk and Pisarczyk [33]), and the record is made on three CCD cameras (2048×2048 pixels, pixel size 7.4×7.4 μm; 16 bits dynamics) placed at 2 m from the vacuum chamber. The magnification of the setup is 2.

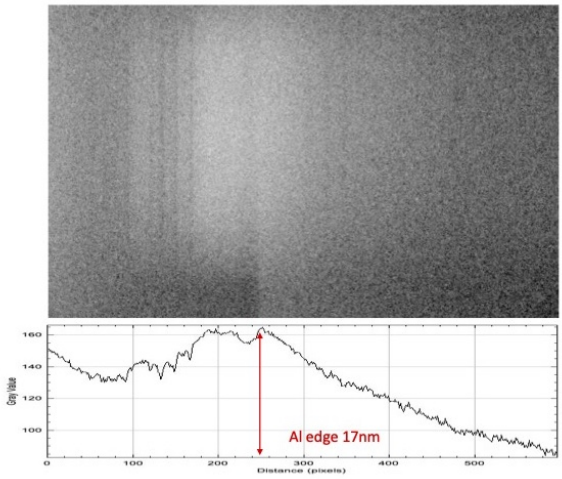

FIG. 2. Row XUV data for the shot 50389 in Argon. In abscissa, the wavelength and in ordinate the image of the channel, are blurred by the poor spatial resolution. The characteristic signature of the Al filter, which covers the back side of the target, is visible at the bottom of the figure.

B. XUV spectroscopy

The time and space integrated XUV emission spectra between 10 to 35 nm have been recorded employing a flat field XUV spectrometer using a concave gold coated VLS grating (curvature radius of 5649 mm, 1200 grooves per mm, efficient grating area of 45 × 27 mm, blaze angle 3.7°). For the detector, an Image Plate (BAS-IP TR 2040) is placed at a distance of ∼ 240 mm from the grating, which is itself located at a distance of ∼ 320 mm from the target. IP detectors have an advantage (over the CCD) to be less sensitive to the hash environment (EMPs) and can be used without protecting film. The spectrometer was installed on the top of the vacuum chamber (figure 1).

An Al filter (0.8 μm) covers part of the noose of the spectrometer corresponding to the field of view of the back side of the shock tube. It provides a useful reference wavelength (sharp edge at 17 - 17.1 nm, figure 2) in the spectrum. This choice allows monitoring on the Image Plate both the spectrum of the shock without the Al filter (part of the target close to the laser impact) and with this filter (back side of the target). It should be noted that the Si_3N_4 window introduces a smoother edge near 12.4 nm[34]. There is no additive angular limitation than the section of the XUV windows of the targets.

III. INTERFEROMETRIC RESULTS

For a given gas, low pressures are more favorable to the development of an extended but weaker radiative precursor (due to a reduced absorption), and high pressures are more favorable for the XUV spectroscopic analysis which requires a sufficient number of emitting ions. On the other hand, for the same pressure, the shock velocity should reduce when increasing either the atomic mass (i.e. passing from Argon to Xenon) or increasing the pressure. However, the shock velocity is mostly given by the speed of the laser-driven piston, and thus the mass effect remains marginal compared with the velocity of the ionisation wave (precursor).

In the next section, we will present the general topology (geometry, extension) of the radiative precursor for two different laser spot sizes. The interferometric records will provide the electron density and the precursor velocity for different pressures, laser energies and focal spots. These results will then be compared with numerical simulations.

TABLE I. Division of averaged electron density into eleven bins and their colour representation.

Electron Density Range $\langle N_e \rangle$ ($/cm^3 \times 10^{19}$)	Colour
$0-0.15$	Yellow
$0.15-0.38$	Cyan
$0.38-0.59$	Blue
$0.59-0.74$	Lime green
$0.74-0.89$	Magenta
$0.89-1.04$	Red
$1.04-1.19$	White
$1.19-1.49$	Orange
$1.49-2.23$	Brown
$2.23-7.43$	Pink
$7.43-1.02$	Black

A. A typical topology of the interferometric images

Typical interferometric records for the single shot 50365 with XeHe gas at 0.6 bar and laser energy 144 J (focal spot of ∼ 330 ± 30 μm, thus, intensity ∼ 4.3 × 10^{14} W/cm^2) are presented for three different times (5,17, 29 ns after shock launching) in the figure 3. The laser comes from the left at time 0 and the shock propagates from the left to the right of the tube. For this shot, a quartz obstacle was placed in the right part of the channel. The objective of this obstacle was to check the potential preheating of the quartz windows at distances from the shock. Indeed, a similar experiment has been performed at higher laser intensities and shock velocities showing some preheating of the obstacle[35]. The sharp interferograms trace the low-density radiative precursor, whereas the denser post-shock (on the left) is opaque to the light of the Ti-Saph laser. Traces of glue can be seen on the upper side of the target and on the left side, where the piston is located.

We deduced the line-integrated electron density by measuring the fringe shift to the initial (recorded before the shot) position. A detailed method can be seen in Singh *et al.*[26]. To highlight the variation in electron density with the position, we divided electron density into 10 bins, each of them having a specific color, as indicated in the table I.

The precursor develops longitudinally with time. It first extends rapidly. Then it slows slightly down with time, as can be seen from the longitudinal profiles of $\langle N_e \rangle$ in figure 3 (right panel) plotted at the "symmetry" axis of the precursor along

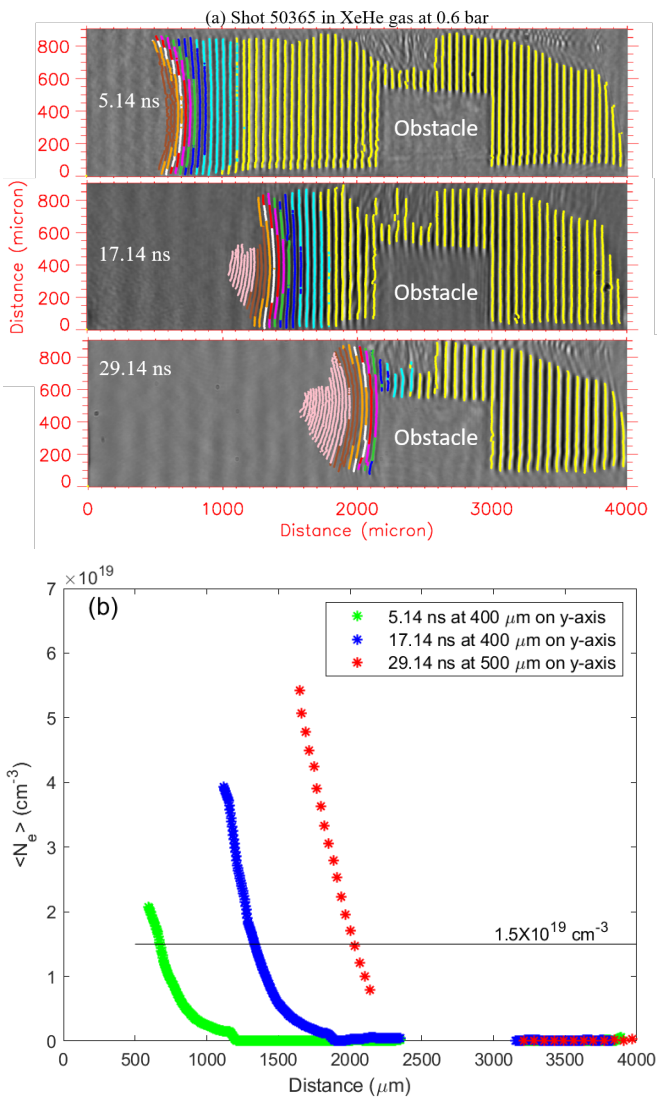

FIG. 3. (a) Recorded 2D shock interferometric images at 5, 17, 29 ns for shot 50365 in XeHe, at 0.6 bar. The laser energy is 144 J, with a focal spot diameter of 330 μm). Traces of glue are visible on the top face of the channel, between $\sim$ 2100 and 2800 μm. (b) The line-integrated electron density ($\langle N_e \rangle$) profiles for the interferometric images is presented at the top. These profiles are plotted at the symmetry axis of the precursor along y. There is no record of the position of the obstacle located between 2350 and 3150 μm.

y (which may slightly differ from the axis of symmetry of the channel). Here, the symmetry axes of precursors recorded at 5, 17 and 29 ns are respectively set to 400, 400 and 500 μms.

At high densities, the plasma becomes more opaque and the contrast of the fringe decreases. They also become very thin and closer to each other. The maximum line integrated electron density, $\sim 6 \times 10^{19}$ cm^{-3}, is about 1/30 of the critical density. Due to the increasing opacity and the confusion in the fringes, it remains difficult to visualize higher electron densities.

In the present example, the radiative shock is unaffected by the obstacle up to 17 ns. There is no evidence of any preheating of the quartz obstacle at the distance of the precursor induced by high-energy radiation. At 29 ns, the radiative precursor is close to the obstacle and is impacted by it for the low-density part. The obstacle itself seems to be unaffected at this time. The following records presented in this study will be performed without any obstacle and will assume the absence of any preheating of quartz windows of the tube ahead of the shock front.

Our interferometric images allow us to measure the speed of radiative heating. This last quantity depends on the value of the average electron density $\langle N_e \rangle$. As long as the precursor extends with time, the lower values of $\langle N_e \rangle$ have a larger velocity than the higher values which are closer to the shock front. For instance, in this record, we deduced velocities at 4, 16 and 29 ns of about 131 km/s (at the launching phase), 78 and 70 km/s stabilization phase respectively for the isocontour $\langle N_e \rangle \sim 1.5 \times 10^{19}$ cm^{-3} in the figure 3(b).

B. Effect of the tight focus

Most of the shots were performed for a focal spot of about 350 μm diameter. However, for Xenon at 0.6 bar, we studied the impact of the focal spot diameter variation on the target. This is obtained through the displacement of the focal lens of the laser. In figure 4, we present typical single-shot 50387 results with laser energy 103 J for Xe gas at 0.6 bar. From the keV camera, the focal spot diameter is then estimated $\sim$ 280 $\pm$30 μm and the intensity is of the order of 4.8×10^{14} W/cm^2 which is comparable to the conditions of the previous shot 50365 (figure 3). The 2D interferometric images were recorded at 4, 16 and 28 ns.

Except for the first snapshot at 4 ns, where the bending of the fringes is more pronounced than in the previous record at 5 ns, and the velocity is higher, the behavior of the precursor at later times is globally similar to the previous one: the radiation flux coming from the shock reaches all the gas inside the channel and the precursor expands laterally. We deduced velocities for shot 50387 (figure 4) at 4 ns, 16 ns and 28 ns of about 169 km/s, 73 km/s and 39 km/s respectively for the isocontour $\langle N_e \rangle \sim 1.5\times10^{19}$ cm^{-3} at the symmetry axis of the precursor.

At large densities, we note that the fringes, which are still visible in the middle of the channel, become less and less visible laterally when the density increases. This could be attributed to residual parasitic diffraction patterns, which superpose to the signal and make it difficult to distinguish from the background. Another explanation could be linked to the slip in the time overlap between the probe and reference beams. Hence, contrarily to the reference beam, the probe beam is deflected in the zones where the plasma is dense and bent. To illustrate this, let us take the ideal case of a uniform cylindrical plasma at a constant electron density inside the channel. The probe laser beam passing through this plasma is deflected two times (at the entrance and the exit of the plasma). For a density of 7×10^{19} cm^{-3} (resp 10^{19} cm^{-3}), this induces a net delay on a detector (placed at $\sim$ 2.5 m from the tube), which is

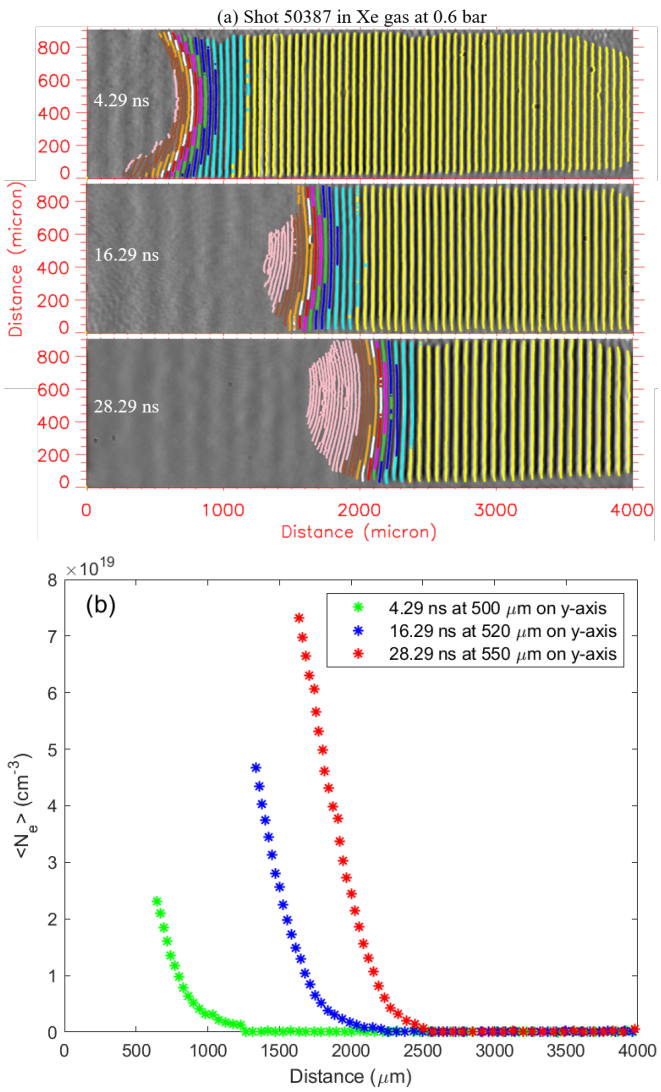

FIG. 4. (a): 2D shock interferometric images at 4, 16, 28 ns for shot 50387 in XeHe, at 0.6 bar. The laser energy for this shot is 103 J and the focal spot is 280 μm. (b): The line integrated electron density ($\langle N_e \rangle$) profiles for the interferometric images presented on the top. These profiles are plotted at the symmetry of the precursor along y.

sufficient to loose the fringes over 10% (resp 30%), see figure 5.

C. Variations with the atomic mass, pressure, laser energy and intensity

To investigate the effects of the pressure and the laser intensity, we will compare in this section six records obtained at different laser energies but for the same spot diameter fixed to $\sim$ 350 μm. To illustrate the effect of the tight binding, we shall in addition also present two shots at 0.6 bar obtained in the tight focus condition (i.e. focal spot $\sim$ 280 μm). The corresponding conditions of the records are summarized in table

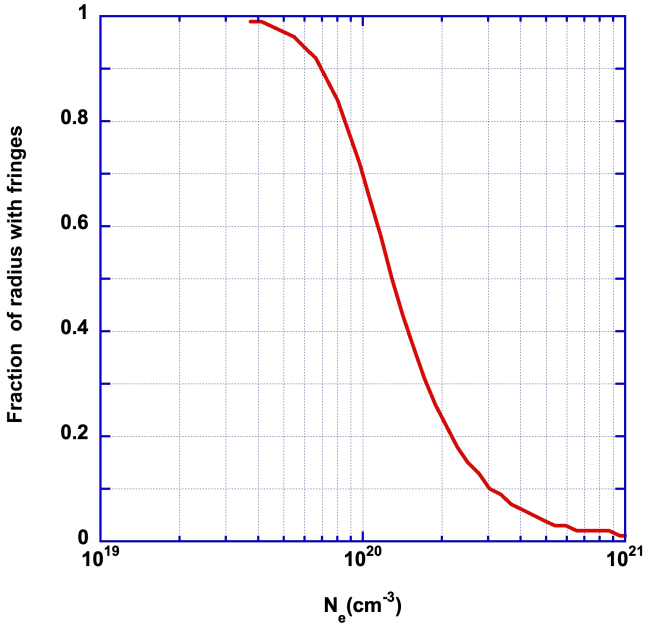

FIG. 5. Fraction of a plasma tube at a uniform electron density N_e, which is covered by fringes. The detector is placed at a distance L = 2.5 m from the plasma cylinder and for the duration of the probing laser pulse is set to 40 fs.

II.

All the interferograms present a similar topology to the previous records (figures 3 and 4), with a smooth bending of the fringes, and a maximum electron density smaller than 7×10^{19} cm^{-3} (pink color), except for the shot 50389 (figure 14b, table II) bin Argon at 0.2 bar in the tight focus (and large laser energy) condition. For this later shot, the fringe pattern remains smooth for densities larger than 10^{19} cm^{-3} (red color). However, below this density, one notes a preionisation under the form of a spike at an early time (4.4 ns), those extension reduces then with time. This shot is also unique to present fringes at densities larger than 7.4×10^{19} cm^{-3}. The corresponding figure 14b is presented in the appendix together with an example of a typical shot in Argon at 0.2 bar.

Comparing Argon at 0.6 bar (shot 50373 at 184 J) and Xenon at 0.6 bar (shot 50364 at 170 J) (see table II), with the same focal spot of 350 μm, we note a faster development in the case of Argon (velocity of $\sim$ 85 km/s versus 60 km/s for Xenon). This may be attributed to a slightly larger laser energy inducing a higher velocity of the shock front. However, a more plausible interpretation is that for similar laser energy, the contribution of the gas opacity, which blocks the XUV radiation coming from the shock and which heats the cold gas, has to be taken into account. The monochromatic opacity of the cold gas being larger for Xenon, the heating wave will be slower for Xenon than for Argon.

Figure 6a presents the time variations of the velocity of the density isocontour equal to 1.5×10^{19} cm^{-3} for the highest pressure (0.6 bar) for Argon and Xenon. Supposing that the gas is only heated and not compressed, this would correspond to an average line integrated ionisation stage equal to unity.

TABLE II. Velocity V in km/s at the latest time in ns for five different shots without any obstacle in the tube. Initial conditions: pressure P (bar), gas nature, mass density ρ (10^{-3}g/cm^{-3}), ion density N_i (10^{19} cm^{-3}), laser Energy E (J), the electron density of the probed isocontour N_e (10^{19} cm^{-3}). The focal spot (μm) of the laser is identical ($\sim$ 350 μm) in these shots except the two last shots 50387 and 50389 ($\sim$ 280 μm, tight focus) in italic.

Shot	Focal spot	P	Gas	ρ	N_i	E	Time	N_e	V
50363	350	0.6	XeHe	3	1.5	95	29	1.5	44
50364	350	0.6	XeHe	3	1.5	170	29.46	1.5	56
50373	350	0.6	Ar	1	1.5	184	28	1.5	88
50381	350	0.2	Ar	0.3	0.5	111	28.68	0.5	75
50391	350	0.2	Ar	0.3	0.5	168	29.06	0.5	103
50387	*280*	*0.6*	*Xe*	*3*	*1.5*	*103*	*28.29*	*1.5*	*39*
50389	*280*	*0.6*	*Ar*	*1*	*1.5*	*134*	*28.4*	*1.5*	*57*

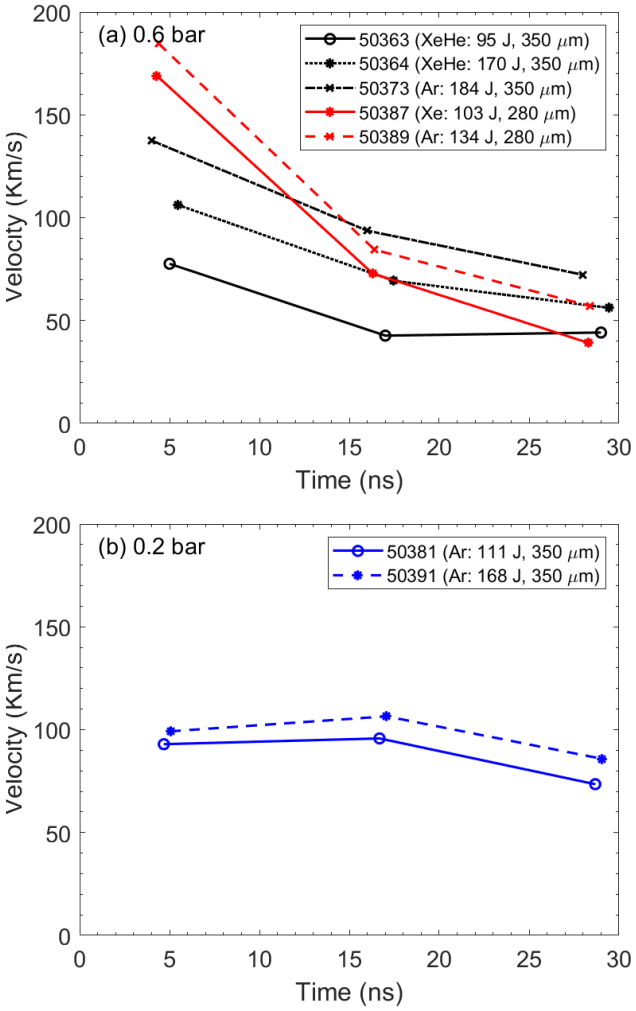

FIG. 6. Velocities of isocontours 1.5×10^{19} cm^{-3} (a) and 0.5×10^{19} cm^{-3} (b) at three different times for selected Xe, XeHe and Ar shots. All the shots were performed with focal spot $\sim$ 350 μm except shots 50387 and 50389 ($\sim$ 280 μm, tight focus, in red color).

As expected, for all the cases, the precursor develops more rapidly at the highest energy (both in position and extension).

The case of Argon at the lowest density of 0.2 bar is more surprising as can be seen from figure 6b. Hence contrarily to the previous cases, the velocity stagnates or even increases slightly up to 15 ns, and decreases after this time. For this pressure, we considered the isocontour at 0.5×10^{19} cm^{-3} to keep the ion stage equal to unity to compare with results in figure 6a. We believe this slow ionisation during the first times is due to an opacity three times lower due to the lower pressure. Hence, it takes more time to ionize the gas at the same ionisation stage. After some time, the absorption of the pre-shock gas increases with the temperature and thus an increasing opacity (as shown from 1D simulations in figure 7, whereas the number of photons coming from the region close to the front tends to decrease with the shock temperature itself. As a consequence, the ionisation wave tends to slow down globally.

The previous discussion was dedicated to comparing shots with the largest focal spot ($\sim$ 350 μm). The tight focus case described by shots 50387 (figure 4) in Xenon and 50389 (figure 14b) in Argon, is globally similar. The major difference concerns the higher velocity in the first instants for the tight focus. Taking the case of Xenon as an example, the first velocity is equal to 169 km/s at 103 J, whereas it was equal to 106 km/s at even higher energy 170 J for shot 50364 (see table II). This is obviously due to the highest local intensity of the laser. However, as it expands more laterally, the velocity decreases faster in the tight focus case (shot 50387), to reach at the last instant 39 km/s to be compared with 56 km/s for shot 50364.

The summary of the estimation of the velocity at the latest time $\sim$ 30 ns is presented in table II for the case of a 350 microns focal spot, for different gases, laser energy and pressure. The results show again that for the same gas and at the same pressure, the velocity increases with laser energy and decreases with the pressure. They also confirm that at constant pressure, the ionisation velocity decreases with increasing atomic mass.

IV. NUMERICAL MODELING OF THE SHOCK STRUCTURE AND DYNAMICS:

The interferometric setup provides an upper limit to the shock velocity. Taking the values at 1.5×10^{19} cm^{-3} in the precursor, this value is comprised of between 40 to 90 km/s depending on the case (see table II). The following numerical analysis will allow for precise the expected temperature and ionic stages of the plasma, quantities which will be of interest for the XUV spectroscopy (Section V B).

A. A qualitative analysis with HELIOS 1D

1D radiative hydrodynamic simulations are useful at first glance to get qualitative information about the shock structure: the existence of a precursor, compression, typical elec-

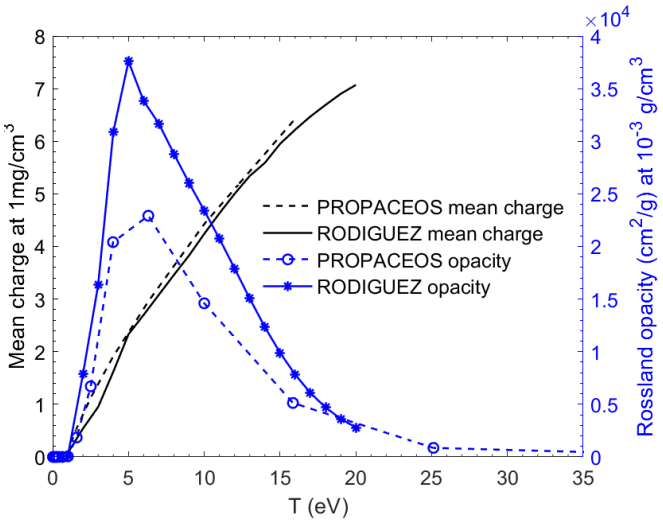

FIG. 7. Variations with the temperature of the Rosseland opacity (in blue) and mean charge (in black) for Argon computed with PROPACEOS and our (RODIGUEZ) models.

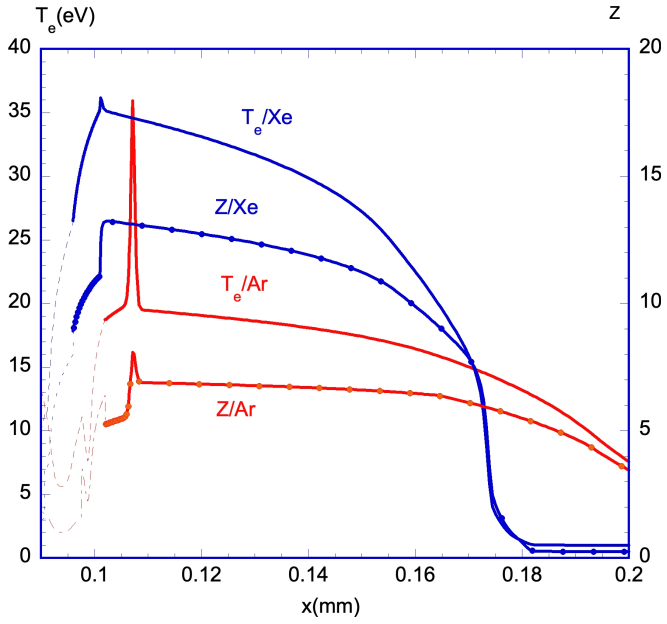

FIG. 8. Electron temperature and mean charge for Argon and Xenon obtained with HELIOS software at 15 ns for E/S = 50000 J/cm^2. Initial pressure 600 mbar. The front shock is located at 0.101 cm for Xenon and 0.107 for Argon and the interface between the gas and the piston are respectively at 0.097 mm and 0.102 mm.

tron density etc. Such simulations have been performed with the HELIOS software[36] and associated PROPACEOS opacities and equation of state.

We present in figures 7 the variations of the Rosseland opacities and the mean charge for Argon at a density of 1 mg/cm^3 versus temperature in eV for the PROPACEOS model and the model computed following the method described for Xenon in Rodriguez *et al.* [29]. Whereas we note a good agreement for the mean charge between the two models, there is a discrepancy of a factor of about 2 between the two opacities. Thus, in the Helios computations presented below, the opacity will be multiplied by 2 for Argon and by a factor of 20 for Xenon[26].

The typical variations of the electron density temperature, mean ion charge and electronic density are reproduced at 15 ns for Argon and Xenon at 600 mbar (figure 8). We are using the temporal profile of the PALS driving laser. The laser energy is set to 50000 J/cm^2 to provide a shock velocity of $\sim$ 70 km/s. This value is below the nominal value for a laser at $\sim$ 100 J, focused over 350 μm, which would lead to an overestimation for Argon and Xenon at 600 mbar, for a shock velocity of $\sim$ 70 km/s of the shock velocity with the available data provided by the software. The simulations are performed with 10 groups of frequencies. The variations of the precursor electron density, which are of interest to the present study can be easily deduced from the mean charge using the relation $N_e = Z^*N_i$, where N_i is reported in table II reported for Argon and Xenon at 600 mbar (table III).

The temperature profile is smoother in Argon than in Xenon, and the temperature is lower due to a larger radiative mean free path. Due to radiation effect and ionisation, the compression at the shock front is large (20 for Argon and 16 for Xenon) compared to the factor of 4 obtained for the adiabatic shock wave[1].

The simulation favors a supercritical regime which means that the electron temperature just before and just after the discontinuity (near 0.1 cm) are equal. The nominal values of the temperature, electron density, and mean charge are reported for Argon and Xenon at 600 mbar (table III).

TABLE III. Typical values for the shock from HELIOS simulations for Argon and Xenon at 600 mbar, for a shock velocity of $\sim$ 70 km/s

	Z	**N_e**	**T_e(eV)**	**rho (g/cm3)**
Ar Precursor	<7	< 1E+20	<20	0.001
Ar Post shock	<6	2E+21	20	0.02
Xe Precursor	<13	< 2E+20	< 35	0.003
Xe Post shock	11	3E+21	30	0.06

In the case of Argon at 200 mbar, the shock is weaker. The front is at about the same position (0.11 cm) as at 600 mbar. The extended precursor is heated at a temperature between 13 eV just before the front and still up to 5 eV at 3.5 mm, close to the tube end, whereas the maximum mean charge is equal to 6. The electron density peaks at 3×10^{19} cm^{-3} just before the shock discontinuity and reaches 9×10^{20} cm^{-3} in the postshock.

B. 2D simulations

We performed numerical simulations of the experiment with the 2D adaptive mesh refinement (AMR) radiative hydrodynamics code ARWEN[37]. This code has been used previously to successfully simulate the formation of a radiative shock wave[15] and other Laboratory Astrophysics systems[?].

The ARWEN code includes a high-order Godunov method for multimaterial hydrodynamics, a diffusion solver for electron heat conduction, a multigroup radiation transport solver and a model for laser energy deposition. The Equations of State used in the simulations is based on the QEOS model fitted to experimental data[38] and the opacities were generated with the BigBART code[39]. For these simulations, we collapsed the spectral opacities into 8 groups.

The target was modelled as an aluminum tube of the inner radius of 300 µm and length 950 µm filled with Xenon gas at 3.1×10^{-3} g cm^{-3} or with Argon gas at 1.0×10^{-3} g cm^{-3} (both corresponding to a pressure of 0.6 bar). Laser energy is 100 J at 433 nm and FWHM of 350 ps with Gaussian temporal profile. The spot diameter of the laser is 330 µm with a hypergaussian profile. Simulation conditions are similar to the experiments shot 50387 (figure 4) for Xenon except for the laser spot size which is (280 ± 30) µm. In figure 9 we show electron density and electron temperature profiles for the Xenon simulation from the average of the 2D results around the axis of the system. We can appreciate from the electron density and temperature profiles that the precursor is very stable after its formation at around 5 ns after the laser irradiation. The average density of the shocked Xe behind the shock is 0.047 g cm^{-3} which makes a compressibility ratio of 14 9.

In figure 10 we show the comparison of the electron temperature for the simulations with Argon and Xenon as filling gas, using as reference for the position along the system axis the position of the shock wave. The only difference in the simulation parameters between both cases is the density of the filling gas, selected to match an initial pressure of 0.6 bar for Argon and Xenon. We tracked the shock wave position with the average of the system properties in a volume around the axis. The averaged shock wave velocity for Argon is 64.5 km s^{-1} and for Xenon 55.7 km s^{-1}. Peak electron temperature ranges from 18.3 eV to 22.1 eV in Argon and from 23.9 eV to 25.8 eV in Xenon, leading to ionization states around Ar^{+6} and Xe^{+9} respectively. As expected, these temperatures are lower than the results from 1D simulations shown in figure 8 due to the consideration of the radiative lateral loses of the radiative shock in 2D. We appreciate from the isocontours of electron density that the precursor in Xenon is much larger than in Argon. The simulations present a larger curvature of the shock wave compared to the experimental as shown in data in figure 14.

We compared the simulation in Xenon with the experimental results of shot 50364. This shot has the closest conditions to the parameters of the simulation and inside the experimental uncertainties related to laser energy and laser spot size. Also, it presents a shock wave velocity similar to the results in the simulation. In figure 11 we show the line integrated electron density ($\langle N_e \rangle$) profiles compared to the ones from the interferometric images. The experimental electron density profile for 5.0 ns is not well reproduced by the simulations but the profile for 17 ns is in agreement with the experiments. The comparison for electron densities in the order of 1.0×10^{19} cm^{-3} is limited due to the unrealistic high ionization in the simulations at low temperatures. Furthermore, the reduced number of energy groups for the radiation transport calculations may affect the shape of the precursor.

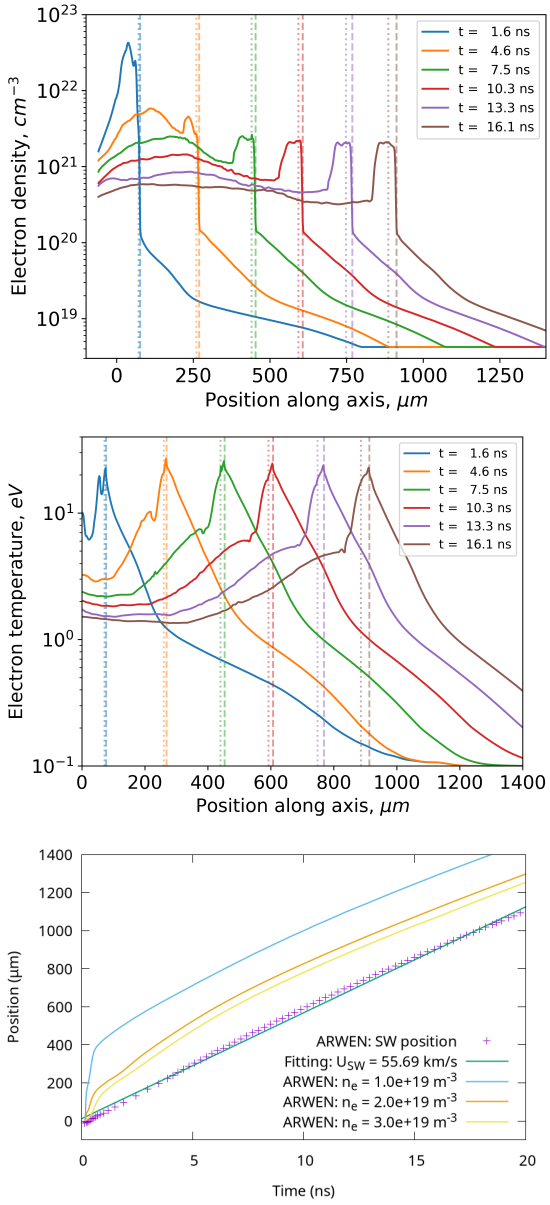

FIG. 9. Results of the 2D simulations in Xenon with ARWEN. We show the averaged profiles around the axis for a radius of 17.5 μm for electron density, electron temperature and the position of the shock wave (SW). For electron density and electron temperature, we show the shock wave position with dashed lines and the interface between the gold plate and the Xe with dotted lines. 2D simulation results from cylindrical target of radius 300 µm and length 950 µm filled with Xe gas at 0.6 bar. Laser energy is 100 J at 433 nm and spot diameter is 330 µm. The EOS model used in the simulations overestimates the ionization state for low temperatures (in this case $Xe^{+0.29}$ at the initial conditions), resulting in a minimum of electron density of 4.2×10^{18} cm^{-3} for the simulations. As expected, the peak electron temperature is achieved just behind the shock wave in the compressed Xe gas.

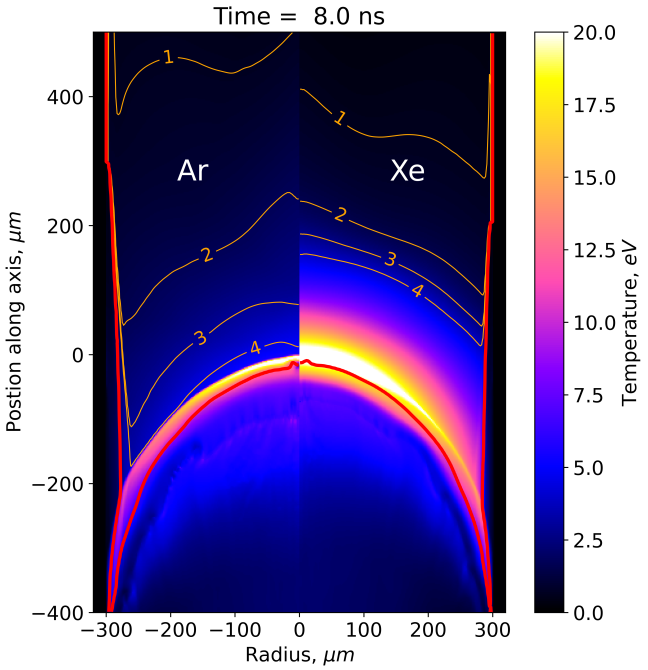

FIG. 10. Comparison of the simulations of radiative precursor in Argon (left) and in Xenon (right) at 8 ns. The orange lines are the isocontours of electron density of 1×10^{19} cm^{-3}, 2×10^{19} cm^{-3}, 3×10^{19} cm^{-3} and 4×10^{19} cm^{-3} and the red line is the material interface between the filling gas and the gold plate. The shock wave front is ahead of the material interface (above the red line). The position along the symmetry axis refers to the shock wave position at the axis for each case. Target and laser parameters are the same for both cases. Also, the pressure of the filling gas is 0.6 bar for Ar and Xe. The oscillations in the electron density isocontours of 1×10^{19} cm^{-3} and 2×10^{19} cm^{-3} are produced by the numerical method of the radiation transport solver and are not physical.

Future work in simulations should include removing these restrictions for a better description of the radiative shock and its precursor.

V. XUV SPECTRA OF RADIATIVE SHOCKS IN ARGON AND XENON

A. A qualitative overview

A qualitative analysis of the expected spectroscopic records has been performed using the PrismSPECT[40] software. It shows that in the conditions of the radiative shock (i.e. T $\sim$ 10-30 eV), NLTE effects are negligible at the post-shock densities ($\rho \sim 1.5\times 10^{-2}$ g/cm^3) and start to be seen for very few lines at the lower densities and higher temperatures. This justifies the LTE assumption used for the HELIOS radiative hydro-simulations.

The emissivity of a thin layer (50 μm thick) of plasma at uniform density and temperature is reported in figure 12 at two temperatures (10 and 30 eV) for Argon at 0.001 and 0.015 g/cm^3, between 5 and 30 nm.

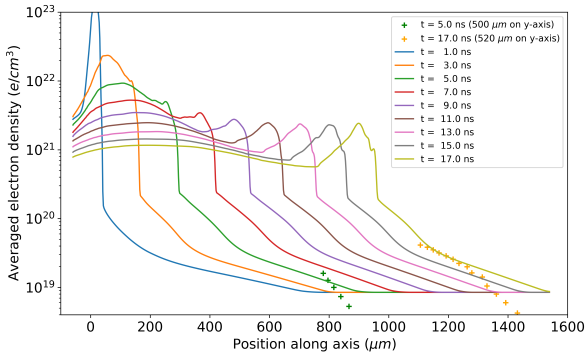

FIG. 11. Integrated electron density from the Xenon simulation compared with experimental data for shot 50364. The comparison is limited due to the effect that simulations have a lower bound for the electron density as mentioned in figure 9. The simulation matches the position of the precursor.

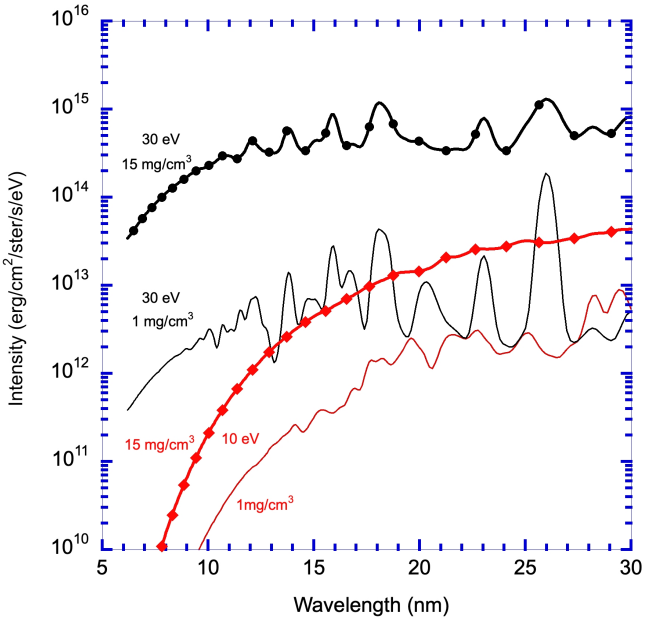

FIG. 12. Emissivity of an Argon plasma with a thickness of 50 μm, obtained with PrismSPECT at LTE for two temperatures (10 eV in red, and 30 eV in black), and two mass densities (0.001 g/cm^{-3} and 0.015 g/cm^{-3}). The plots corresponding to the higher density are identified by symbols. The resolution $\lambda/\Delta\lambda$ is set to 40 for simplification.)

One may first note that the spectrum is richer in lines at the highest temperature. In addition, the relative contribution of the continuum increases with the mass density. At 30 eV (resp 10 eV), the intensity is about 100 times (resp. 10 times) higher for the highest mass density than for the lowest one.

However, the denser post-shock has a more minor extension than the low-density precursor, thus the contribution of the latter to the space and time-integrated data cannot be neglected at first glance.

In addition, as expected by the presence of a radiative precursor, the emerging spectrum is affected by radiation transfer effects[41]. Thus, to collect the maximum of photons on the detector, it is then suitable to reduce the thickness of the cold gas layers between the shock and the detector[22].

B. XUV spectroscopic Experimental results

As indicated previously, the wavelength calibration is performed using the Al edges in the first and second orders using different records, the dispersion rule for an aberration-corrected concave grating[42,43], and some adjustments[44].

Contrary to our previous experiment[26] using together a CCD camera and an Aluminium filtering covering all the radiation of the target, the records are here wider in terms of wavelengths. It extends from 10 to 35 nm.

In the present case, the absence of an Aluminium filter that blocks the light below 17 nm introduces the complication of the contribution of the different diffraction orders in the net spectra. This is why we shall limit our study to wavelength comprised between 10 and 22 nm, where the signal is at maximum.

We present below the results obtained for Argon (shot 50389; laser energy 134J) and Xenon (shot 50382; laser energy 183J) at 0.6 and 0.5 bar respectively. In these shots, the laser focalisation is similar to the one used previously for shot 50387 (tight focus, section III B). High intensity, relatively high pressures and a focalisation slightly centered upwards on the tube (to reduce the absorption by the gas) are necessary to obtain at least a moderate-quality signal.

The recorded spectra, presented in figure 13, are composed of a multitude of relatively faint lines superposed to a strong continuum, which is expected from the contribution of the denser post-shock and also from the heated CH-Au material behind the shock. However, our purpose is not to identify all these lines but some of them to deduce information about the ionisation stages present in the plasma.

Our procedure takes advantage of the presence of Oxygen lines in the Argon and Xenon spectra. Thus, to help with the determination, we first compute as a reference the monochromatic opacity of Argon and a mixture of Argon with Oxygen in conditions reasonably close to the experiment (1 mg.cm^{-3} and 15 eV). These monochromatic opacities are computed with PrismSPECT[40] software, which for Argon, gives line positions, in agreement with the NIST database[45]. The differences between the 2 monochromatic opacities are unambiguously accredited to Oxygen lines. Among them, we retain only those which are also present in the Ar and Xe experimental spectra. The corresponding lines are attributed to OV and OVI, which is coherent with a plasma at 15-30 eV.

After this stage, we focus our attention on the lines present in the Ar spectrum and not in the Xe spectrum. For Argon, with the help of the previous monochromatic opacities and also of the NIST database, the residual lines are mostly ascribed to Ar^{7+}. Few lines are attributed to Ar^{6+} and $^{8+}$ in agreement with an ionisation stage comprised between 6 and 8. This is consistent with a plasma comprised of between 15 and 30 eV. Assuming that the density of the radiatively heated precursor remains equal to its unperturbed value, these values are consistent with an electron density reaching local values in the range of 10^{20} cm^{-3}.

The situation of Xenon is more complex, due to its rich spectrum. However, the lines, which we have identified using the NIST reference data, are assigned to Xe^{7+}, Xe^{8+}, Xe^{9+}, and Xe^{10+}, with a possible line at 11.3 nm which can be attributed either to Xe^{10+}or Xe^{6+} (1 line). This is consistent with an ionisation stage between 7 and 10, corresponding to an electron density between 1-1.5 $\times$ 10^{20} cm^{-3}, in agreement with the interferometric measurement (figure 14b).

VI. SUMMARY AND PERSPECTIVES

In conclusion, we have performed a detailed comparative study of the topology, dynamics and electron density of radiative precursors developing in two noble gases, Argon and Xenon, at two initial pressures (0.2 and 0.6 bar). This study was obtained due to high-quality targets, and a time-resolved instantaneous imaging setup using a based femtosecond laser, which was used for the first time in such circumstances. This setup presented high-quality images without blurring and with a high fringe contrast. It showed its interest in future radiative shock experiments at higher velocities. It was also shown that even small deflections of the probing laser beam, compared to the reference beam, induced by high-density electron bent zones may lead to the disappearance of the fringes. This unexpected effect, together with a precise measurement of the initial time overlap, and of the distances of interest, could be used as an auxiliary indicator of the bent shape of the plasma. We would like to point out the good reproducibility of the records which could not be presented in detail. In addition, we proved the feasibility of the use of image plates as a detector in the XUV range. Even if a new plate was used at each shot, these cheap detectors, compared to CCD, present the advantage of being insensitive to EMP and to residual IR laser light visible light. Thus they don't need to be protected by additive filters. As a consequence, we recorded for the first time the spectra for the two gases, from 10 to 30 nm. Many lines were identified. The interferometric records were interpreted due to the combination of 1D simulations, as a first insight and 2D simulations for more detailed analysis.

The interferometric images show a bending in the precursor from Argon and Xenon, whatever the initial pressure. For the same initial laser conditions and gas pressure, the precursor extension is longer for Argon than for Xenon. This is due to the larger light absorption mean free path for Argon than for Xenon over the temperature domain.

An interesting point concerns Argon at 0.2 bar, where it was shown that contrarily to the case at higher pressure, and to the Xenon case, the precursor velocity is almost constant (or even slightly increases) over the first 15 nanoseconds, and then decreases with the time. This behavior is not expected in the case of a constant opacity, where the velocity decreases monotonically with time. We believe that this is a direct consequence of the opacity, and needs to be confirmed in future

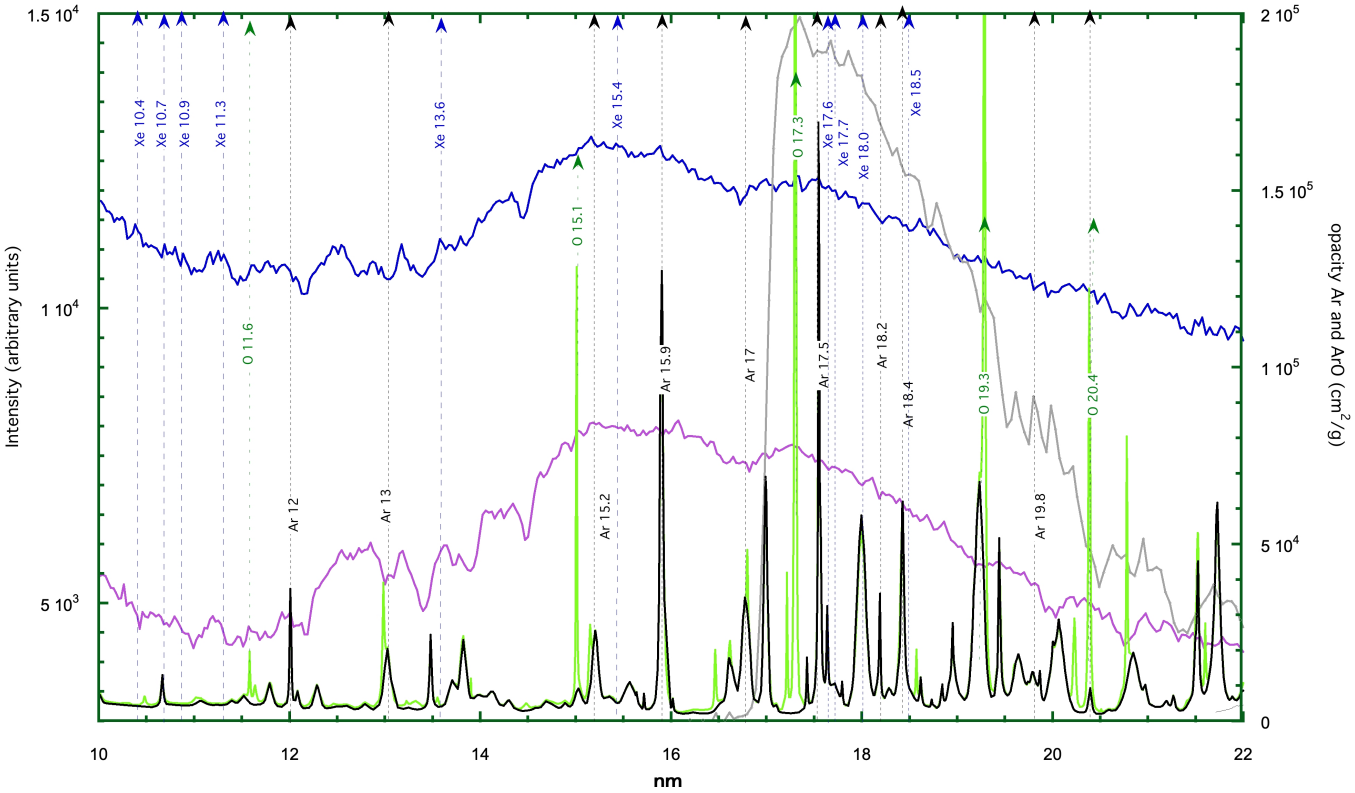

FIG. 13. Time and space integrated XUV spectra of Argon (shot 50389; in pink) and Xe (shot 50382; in blue) between 10 and 22 nm. The interval between two pixels corresponds to $\sim$ 0.04 nm, and the spectral resolution $\sim$ 0.05 nm near 15 nm. A previous record of Xenon (shot 48143; in gray) is presented for comparison[26]. The monochromatic opacity obtained with PRISMSPECT software, at LTE, for Ar (in black) and Ar(90%)-O(10%) (in green), both at a mass density of 1mg/cm^{-3} and a temperature of 15 eV) are reported for information.

works.

Another interesting result is that, when the energy is concentrated in a smaller focus (tight focus case), we note a higher velocity at an early time, but a lower one at longer times. This is due to a stronger bending of the shock, which loses more energy laterally. However, the extreme case of a blast wave, where the laser energy is concentrated in a small focal spot, presents the advantage of a simpler symmetry (1D spherical) and a negligible contribution of the lateral windows of the target, supposed to be at a larger distance than in the present case.

The 2D simulations show good stability of the radiative shock wave after its formation for both Argon and Xenon cases, keeping the velocity of the shock wave almost constant over the time span of the analysis. Xenon exhibits a more intense coupling between hydrodynamics and radiation transport thus producing a radiative shock wave with higher temperatures and a much larger precursor than in Argon although the Argon simulation has a higher shock wave velocity. At later times, the shock wave front becomes unstable for both cases and we need further analysis to study its effect on the precursor.

This work shows the advantage of using Argon as a template for experimental radiative shocks in place of Xenon. Indeed, due to its simpler ionic structure, the opacity and equation of state are, in practice, more precise than for Xenon. It goes also for the spectroscopic signatures. This eliminates the important difficulty of the opacity accuracy in the radiative hydrodynamics simulations. As a consequence, they are more adapted if the goal is to test the quality of radiative hydrodynamic simulations, which remains today a difficult challenge. The use of Argon and Ar-O mixture would even help more for the line identification and wavelength calibration.

Despite the absence of space and time resolution, the analysis of the spectra is a good indicator of the ionic stages obtained in the shock. The spectra are rich in lines. However, the presence of Oxygen lines and the comparison of the Xenon and Argon spectra allow line identification. Oxygen is present as O V and O VI (which is coherent with a plasma at 15-30 eV), and Argon is present as Ar VII, VII and IX, which is also coherent with the same temperature range.

This work shows that challenging spectroscopic investigations become feasible with adequate instrumentation. We hope that these preliminary results will facilitate future studies at the higher spectral resolution, which would facilitate the identification of the lines over the strong continuum. The next step should be to implement spatial and time resolution, which will require a new generation XUV spectroscopic diagnostic.

VII. ACKNOWKEDGEMENTS

C. Stehlé acknowledges the support from the Labex Plas@Par (ANR-11-IDEX-0004-02), the Programme National de Physique Stellaire of CNRS/INSU, Observatoire de Paris, and PALS (Prague Asterix Laser System). Thanks to the Czech Ministry of Education, Youth and Sports (CMEYS) for the financial support of the project nr. LM2023068. R. Rodriguez acknowledges the support of the Spanish Government through the project PID2019-110678GB-I00. M. Cotelo and P. Velarde acknowledge the support of the Spanish Government through the project PID2021-124129OB-I00 funded by MCIN/AEI/ 10.13039/501100011033/ERDF, EU. We thank J. Larour (retired from LPP, CNRS, Ecole Polytechnique, Sorbonne-University, France) for his support during the experiment. We thank Tomasz Chodukowski (Institute of Plasma Physics and Laser Microfusion, Warsaw) for taking part in a few discussions related to interferometric data analysis.

VIII. APPENDICES

We present here two interferometric images for Argon at 200 mbar under different laser conditions for the energy (respectively 111 J and 134 J) and focalisation (respectively 350 μm and 280 μm diameter). They illustrate the influence of the laser intensity on the development of the precursor (Section II A).

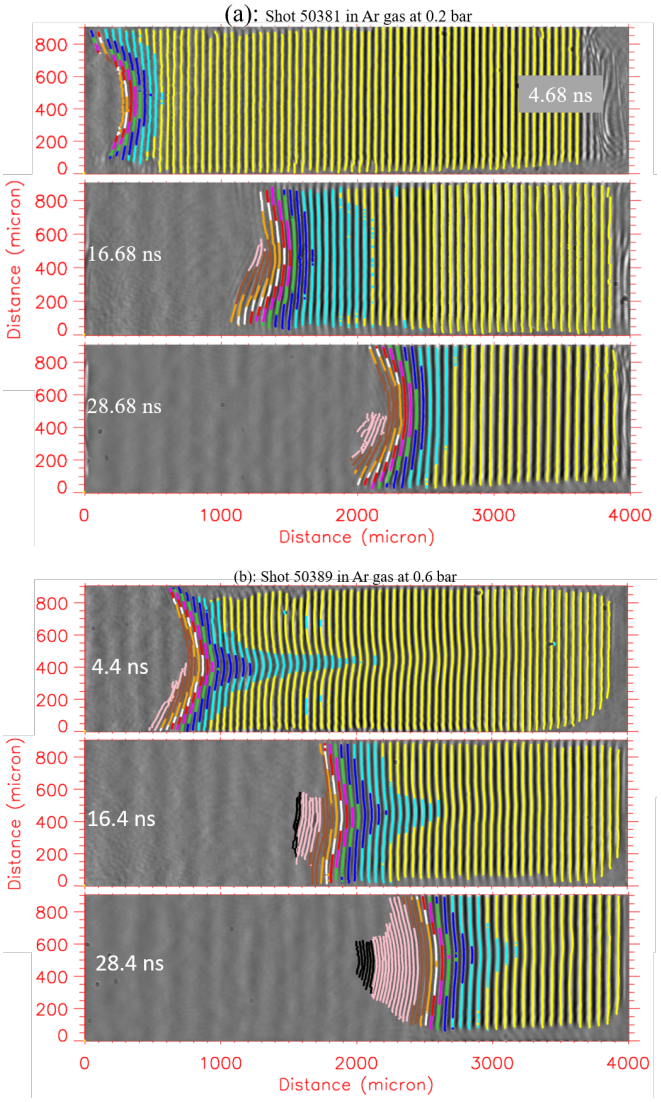

FIG. 14. (a): shot 50381 with 111 J laser energy for Ar gas at 0.2 bar and images are recorded at 4.68, 16.68, 28.68 ns. (b) Shot 50389 with 134 J laser energy and spot size for this shot is $\sim$ 280 μm for Ar gas at 0.6 bar and images are recorded at 4.4, 16.4, 28.4 ns.

[1] C. Michaut, C. Stehlé, S. Leygnac, T. Lanz, and L. Boireau, "Jump conditions in hypersonic shocks," The European Physical Journal D-Atomic, Molecular, Optical and Plasma Physics **28**, 381–392 (2004).
[2] Y. B. Zel'Dovich and Y. P. Raizer, *Physics of shock waves and high-temperature hydrodynamic phenomena* (Courier Corporation, 2002).
[3] A. C. Raga, G. Mellema, S. J. Arthur, L. Binette, P. Ferruit, and W. Steffen, "3D transfer of the diffuse ionizing radiation in ISM flows and the preionization of a herbig-haro working surface," Revista Mexicana de Astronomia y Astrofisica **35**, 123 – 133 (1999).
[4] L. de Sá, J.-P. Chièze, C. Stehlé, I. Hubeny, T. Lanz, and V. Cayatte, "New insight on accretion shocks onto young stellar objects: Chromospheric feedback and radiation transfer," Astronomy and astrophysics **630**, A84 1– A84 17 (2019).
[5] S. Colombo, L. Ibgui, S. Orlando, R. Rodriguez, G. Espinosa, M. González, C. Stehlé, L. de Sà, C. Argiroffi, B. R., and G. Peres, "Effects of radiation in accretion regions of classical T Tauri stars: Pre-heating of accretion column in non-LTE regime," Astronomy and astrophysics **629** (2019), 10.1051/0004-6361/201935989.
[6] U. M. Noebauer, S. A. Sim, M. Kromer, F. K. Röpke, and W. Hillebrandt, "Monte Carlo radiation hydrodynamics: methods, tests and application to Type Ia supernova ejecta," Monthly Notices of the Royal Astronomical Society **425**, 1430–1444 (2012), https://academic.oup.com/mnras/article-pdf/425/2/1430/4028303/425-2-1430.pdf.
[7] W. V. Jacobson-Galán, L. Dessart, D. O. Jones, R. Margutti, D. L. Coppejans, G. Dimitriadis, R. J. Foley, C. D. Kilpatrick, D. J. Matthews, and i. Rest, S., "Final moments. i. precursor emission, envelope inflation, and enhanced mass loss preceding the luminous type ii supernova 2020tlf," The Astrophysical Journal **924**, 15 (2022).
[8] D. Mihalas and B. W. Mihalas, *Foundations of radiation hydrodynamics* (Courier Corporation, 2013).
[9] R. P. Drake, "Theory of radiative shocks in optically thick media," Physics of Plasmas **14**, 043301 (2007).
[10] C. Michaut, E. Falize, C. Cavet, S. Bouquet, M. Koenig, T. Vinci, A. Reighard, and R. P. Drake, "Classification of and recent research involving radiative shocks," Astrophysics and Space Science **322**, 77–84 (2009).
[11] R. M. Lowrie, Robert B. Rauenzahn, "Radiative shock solutions in the equilibrium diffusion limit," Shock Waves **16**, 445–453 (2007).
[12] M. W. Sincell, M. Gehmeyr, and D. Mihalas, "The quasi-stationary structure of radiating shock waves. i. the one-temperature fluid," Shock Waves **9**, 391–402 (1999).
[13] B. Fryxell, E. Rutter, and E. S. Myra, "Simulations of laser experiments of radiative and non-radiative shocks," High Energy Density Physics **8**, 141–149 (2012).
[14] M. González and C. Audit, E.and Stehlé, "2D numerical study of the radiation influence on shock structure relevant to laboratory astrophysics," Astronomy & Astrophysics **497**, 27–34 (2009).
[15] M. Cotelo, P. Velarde, A. de la Varga, D. Portillo, C. Stehlé, U. Chaulagain, M. Kozlova, J. Larour, and F. Suzuki-Vidal, "Simulation of radiative shock waves in Xe of last PALS experiments," High Energy Density Physics **17**,

68–73 (2015), 10th International Conference on High Energy Density Laboratory Astrophysics.
[16]S. J. Meng, F. Ye, Z. P. Xu, X. S. Yan, S. Q. Jiang, J. Lu, Z. C. Huang, Q. Yi, F. X. Chen, and R. H. i. Yang, "Visualizing magnetically driven converging radiative shock generated in z-pinch foil liner implosion," Physics of Plasmas **28**, 122713 (2021).
[17]K. Kondo, M. Nakajima, T. Kawamura, and K. Horioka, "Relaxation layer in electro-magnetically driven strong shocks," Journal of Physics: Conference Series **112**, 042028 (2008).
[18]J. Larour, R. Singh, C. Stehlé, A. Ciardi, U. Chaulagain, and F. Suzuki-Vidal, "Optimization of an electromagnetic generator for strong shocks in low pressure gas," High Energy Density Physics **17**, 129–134 (2015).
[19]J. C. Bozier, G. Thiell, J. P. Le Breton, S. Azra, M. Decroisette, and D. Schirmann, "Experimental observation of a radiative wave generated in xenon by a laser-driven supercritical shock," Physical review letters **57**, 1304 (1986).
[20]S. Bouquet, C. Stehlé, M. Koenig, J.-P. Chièze, A. Benuzzi-Mounaix, D. Batani, S. Leygnac, X. Fleury, H. Merdji, C. Michaut, F. Thais, N. Grandjouan, T. Hall, E. Henry, V. Malka, and J.-P. J. Lafon, "Observation of laser driven supercritical radiative shock precursors," Phys. Rev. Lett. **92**, 225001 (2004).
[21]A. B. Reighard, R. P. Drake, K. K. Dannenberg, D. J. Kremer, M. Grosskopf, E. C. Harding, D. R. Leibrandt, S. G. Glendinning, T. S. Perry, B. A. Remington, J. Greenough, J. Knauer, T. Boehly, S. Bouquet, L. Boireau, M. Koenig, and T. Vinci, "Observation of collapsing radiative shocks in laboratory experiments," Physics of Plasmas **13**, 082901 (2006), https://doi.org/10.1063/1.2222294.
[22]C. Stehlé, M. González, M. Kozlova, B. Rus, T. Mocek, O. Acef, J. Colombier, T. Lanz, N. Champion, K. Jakubczak, J. Polan, P. Barroso, D. Bauduin, E. Audit, J. Dostal, and M. Stupka, "Experimental study of radiative shocks at PALS facility," Laser and Particle Beams **28**, 253–261 (2010).
[23]C. Stehlé, M. Kozlová, J. Larour, J. Nejdl, N. Champion, P. Barroso, F. Suzuki-Vidal, O. Acef, P.-A. Delattre, and J. i. Dostál, "New probing techniques of radiative shocks," Optics Communications **285**, 64–69 (2012).
[24]U. Chaulagain, C. Stehlé, J. Larour, M. Kozlová, F. Suzuki-Vidal, P. Barroso, M. Cotelo, P. Velarde, R. Rodriguez, and J. M. i. Gil, "Structure of a laser-driven radiative shock," High Energy Density Physics **17**, 106–113 (2015).
[25]F. Suzuki-Vidal, T. Clayson, C. Stehlé, G. F. Swadling, J. M. Foster, J. Skidmore, P. Graham, G. C. Burdiak, S. V. Lebedev, U. Chaulagain, R. L. Singh, E. T. Gumbrell, S. Patankar, C. Spindloe, J. Larour, M. Kozlova, R. Rodriguez, J. M. Gil, G. Espinosa, P. Velarde, and C. Danson, "Counterpropagating radiative shock experiments on the ORION laser," Phys. Rev. Lett. **119**, 055001 (2017).
[26]R. L. Singh, C. Stehle, F. Suzuki-Vidal, M. Kozlová, J. Larour, U. Chaulagain, T. Clayson, R. Rodriguez, J. Gil, J. Nejdl, *et al.*, "Experimental study of the interaction of two laser-driven radiative shocks at the pals laser," High Energy Density Physics **23**, 20–30 (2017).
[27]F. Suzuki-Vidal, T. Clayson, C. Stehlé, U. Chaulagain, J. W. D. Halliday, M. Sun, L. Ren, N. Kang, H. Liu, and B. i. Zhu, "First radiative shock experiments on the SG-II laser," High Power Laser Science and Engineering **9** (2021).
[28]J. C. Bozier, J. P. Le Breton, T. Jalinaud, and J. Valadon, "A new supercritical shock wave regime," The Astrophysical Journal Supplement Series **127**, 253 (2000).
[29]R. Rodriguez, G. Espinosa, J. M. Gil, C. Stehlé, F. Suzuki-Vidal, J. G. Rubiano, P. Martel, and E. Mínguez, "Microscopic properties of xenon plasmas for density and temperature regimes of laboratory astrophysics experiments on radiative shocks," Physical Review E **91**, 053106 (2015).
[30]M. Koenig, T. Vinci, A. Benuzzi-Mounaix, N. Ozaki, A. Ravasio, M. Rabec le Glohaec, L. Boireau, C. Michaut, S. Bouquet, and S. i. Atzeni, "Radiative shocks: An opportunity to study laboratory astrophysics," Physics of Plasmas **13**, 056504 (2006).
[31]K. Jungwirth, A. Cejnarova, L. Juha, B. Kralikova, J. Krasa, E. Krousky, P. Krupickova, L. Laska, K. Masek, T. Mocek, M. Pfeifer, A. Präg, O. Renner, K. Rohlena, B. Rus, J. Skala, P. Straka, and J. Ullschmied, "The prague asterix laser system," Physics of Plasmas **8** (2001), doi.org/10.1063/1.1350569.
[32]J. Dostal, R. Dudzak, T. Pisarczyk, M. Pfeifer, J. Huynh, T. Chodukowski, Z. Kalinowska, E. Krousky, J. Skala, and J. i. Hrebicek, "Synchronizing single-shot high-energy iodine photodissociation laser PALS and high-repetition-rate femtosecond Ti: sapphire laser system," Review of Scientific Instruments **88**, 045109 (2017).
[33]A. Kasperczuk and T. Pisarczyk, "Application of automated interferometric system for investigation of the behaviour of a laser-produced plasma in strong external magnetic fields," Optica Applicata **31**, 571–598 (2001).
[34]B. L. Henke, E. M. Gullikson, and J. C. Davis, "X-ray interactions: photoabsorption, scattering, transmission, and reflection at E = 50-30000eV, z = 1-92," Atomic Data and Nuclear Data Tables **54**, 181–342 (1993).
[35]M. Koenig, T. Michel, R. Yurchak, C. Michaut, B. Albertazzi, S. Laffite, E. Falize, L. Van Box Som, Y. Sakawa, and T. i. Sano, "Interaction of a highly radiative shock with a solid obstacle," Physics of Plasmas **24**, 082707 (2017).
[36]J. J. MacFarlane, I. E. Golovkin, and P. R. Woodruff, "Helios-CR a 1D radiation-magnetohydrodynamics code with inline atomic kinetics modeling," Journal of Quantitative Spectroscopy and Radiative Transfer **99**, 381–397 (2006).
[37]F. Ogando and P. Velarde, "Development of a radiation transport fluid dynamic code under AMR scheme," Journal of Quantitative Spectroscopy and Radiative Transfer **71**, 541–550 (2001), radiative Properties of Hot Dense Matter.
[38]M. Cotelo, P. Velarde, and C. de la Varga, A. G.and García-Fernández, "Equation of state for laboratory astrophysics applications," Astrophysics and Space Science **336**, 53–59 (2011).
[39]A. de la Varga, P. Velarde, M. Cotelo, F. de Gaufridy, and P. Zeitoun, "Radiative properties for warm and hot dense matter," High Energy Density Physics **7**, 163–168 (2011).
[40]PrismSPect, https://www.prism-cs.com/Software/PrismSPECT/overview.html.
[41]L. Ibgui, I. Hubeny, T. Lanz, C. Stehlé, M. González, and J. Chièze, "3d spectral radiative transfer with IRIS: Application to the simulation of laboratory models of accretion shocks in young stellar objects," Numerical Modeling of Space Plasma Flows (ASTRONUM2012) **474**, 66 (2013).
[42]N. Yamaguchi, J. Katoh, Y. Sato, T. Aota, A. Mase, and T. Tamano, "Space-resolving flat-field vacuum ultraviolet spectrograph for plasma diagnostics," Review of scientific instruments **65**, 3408–3414 (1994).
[43]T. Harada, H. Sakuma, Y. Ikawa, T. Watanabe, and T. Kita, "Design of high-resolution xuv imaging spectrometer using spherical varied line-space grating," in *X-ray and EUV/FUV spectroscopy and polarimetry*, Vol. 2517 (SPIE, 1995) pp. 107–115.
[44]L. Lecherbourg, *Spectroscopie d'absorption ultra-rapide de rayonnement X pour l'étude de la matière en régime transitoire.*, Ph.D. thesis, Ecole Polytechnique X (2007).
[45]A. Kramida, Y. Ralchenko, J. Reader, and N. A. Team, "Nist atomic spectra database (version 5.8) 2020," National Institute of Standards and Technology: Gaithersburg, MD, USA (2020).
[46]M. W. Sincell, M. Gehmeyr, and D. Mihalas, "The quasi-stationary structure of radiating shock waves. I. The one-temperature fluid," Shock Waves **9**, 391–402 (1999).
[47]E. García Saiz, G. Gregori, D. O. Gericke, J. Vorberger, B. Barbrel, R. J. Clarke, R. R. Freeman, S. H. Glenzer, F. Y. Khattak, M. Koenig, O. L. Landen, D. Neely, P. Neumayer, M. M. Notley, A. Pelka, D. Price, M. Roth, M. Schollmeier, C. Spindloe, R. L. Weber, L. van Woerkom, K. Wünsch, and D. Riley, "Probing warm dense lithium by inelastic x-ray scattering," Nature Physics (2008).